Ocean Engineering 292 (2024) 116577

Contents lists available at ScienceDirect

Ocean Engineering

journal homepage: www.elsevier.com/locate/oceaneng

Numerical modelling of a 1.5 MW tidal turbine in realistic coupled wave–current sea states for the assessment of turbine hub-depth impacts on mechanical loads

Callum Guy [a,*], Edward Hart [b], Venugopal Vengatesan [a], David Forehand [a]

[a] School of Engineering, Institute of Energy Systems, The University of Edinburgh, Edinburgh, EH9 3DW, UK
[b] School of Engineering, Department of Electronic and Electrical Engineering, The University of Strathclyde, Glasgow, G1 1XQ, UK

ARTICLE INFO

Keywords:
Tidal turbine
Wave–current
Computational fluid dynamics
Marine energy

ABSTRACT

This paper considers hub-depth impacts on mechanical loads for a tidal turbine operating in realistic coupled wave–current sea states. A novel medium-fidelity actuator-line CFD model for simulating tidal turbine non-steady hydrodynamic rotor load responses in the presence of turbulence, shear, and surface waves is developed. The model is validated using tank testing data from a lab-scale turbine. The validated model is then upscaled, to a power rating of 1.5 MW, and simulated in realistic wave–current conditions consistent with those of the MeyGen site. Mean torque and thrust are found to increase with turbine hub height, and the presence of waves is shown to increase mean torque and thrust values by up to 22% and 11%, respectively. The effect on standard deviations and maximum values for these variables is more pronounced, with increases of up to 2500% and 1700% in signal standard deviations, and up to 80% and 30% in maximum values for torque and thrust, respectively. The presence of longer period waves is also shown to reduce mean torque levels, while the corresponding standard deviations and maximum values remained relatively unchanged. In such circumstances, the turbine is operating with an undesirable combination of low-power and high-fatigue. Tidal turbine hub loading characteristics and sensitivities, in the context of the operational loads which subsequently enter the drivetrain and turbine support structure, are also analysed. The magnitude of out-of-plane rotor moments are found to increase with the hub height and wave height. Complex flow interactions are shown to play an important role in this context, leading to what is termed "wave-driven moment-type dominance" effects. Overall, both the rotor location and wave composition are found to significantly impact the turbine's rotor mechanical load response.

1. Introduction

Scotland is blessed with a large, predictable natural resource; tidal streams. Conservative estimates suggest a single location, the Pentland Firth, could produce half the countries electrical demand Draper et al. (2014). Tidal streams are extremely reliable and can be forecast many years into the future, making tidal stream turbines an attractive avenue for green energy investment that could aid in providing security of supply within future energy networks (Clarke et al., 2006). Because of this, Scotland has been able to position itself at the forefront of research and development in tidal stream turbine technology, with significant investment made in the sector over the last decade. Current commercial developers such as Nova Innovation, Orbital Marine, and SIMEC Atlantis Energy have all identified Scotland as a base from which to centre their operations.

Scotland's first grid connected tidal stream turbine was OpenHydro's 250 kW open-centre machine, which was deployed in 2008 at the European Marine Energy Centre (EMEC). EMEC has since seen numerous installations of full scale tidal stream turbines such as Atlantis' AR1000 1MW machine in 2011, Alstom's 1MW machine in 2013, and more recently the world's most powerful tidal turbine, Orbitals 2MW SR2000 in 2016 (later replaced by the O2 in 2021). Though tidal stream energy converters have the potential to take numerous forms, full scale devices have tended towards bladed rotors that bear resemblance to wind turbines. At present, there are few tidal devices contributing to the UK energy network as a whole. The largest capacity project, MeyGen, comprising 4 1.5MW SIMEC Atlantis turbines, started exporting electricity to the UK grid in 2016 and the connection of Orbital Marine's 2MW O2 in 2021, at the Fall of Wareness site, make

* Corresponding author.
E-mail address: callum.guy@ed.ac.uk (C. Guy).

https://doi.org/10.1016/j.oceaneng.2023.116577
Received 6 June 2023; Received in revised form 12 June 2023; Accepted 12 December 2023
Available online 16 December 2023

up the major penetration of tidal to the UK grid. However, other projects such as The Shetland Tidal Array, currently an array of 4 Nova Innovation 600 kW turbines, has been delivering electrical power to homes and businesses on the island of Shetland since 2016. A recent UK Government Contract for Difference (CfD) auction allocated contracts for 41MW between four new tidal stream projects, which will include £20 million of support per year. The contracts will see the MeyGen project expand by 28MW, and the deployment of a further 3 O2 devices, taking Orbital Marine's in-service capacity to 9.2MW. Together, this would result in the UK's installed tidal capacity exceeding 51MW by 2027, producing enough clean energy to supply approximately 74,000 homes a year. This would constitute a strong start in a period of commercialization for the industry, however, with the current lack of in-service experience and data, unforeseen challenges will likely arise and need to be resolved.

With respect to tidal stream devices themselves, tidal turbines are a less established technology than their cousin wind turbines. Whereas wind turbine technology has now essentially converged to three-bladed pitch-regulated machines, optimal design for tidal devices remains an open question. Furthermore, given the differences in the operational environments of wind and tidal turbines, it may be that optimal design for a tidal device is different to that of a wind turbine. While this may be the case, currently deployed tidal turbines do share a number of similarities with modern wind turbines. This includes similar drivetrain setups, where the rotor connects to a main shaft, supported by one or more main bearings, which then possibly feeds into a gearbox and then into an electromagnetic generator. Another key similarity between tidal turbines and offshore wind turbines is the support structure. Both technologies may be bottom-fixed or floating. For wind turbines this distinction does not generally result in a change in hub height and thus the rotor location within the flow field, however, where tidal turbines are concerned this may influence the rotor's position in the water column. Generally, when re-configuring a tidal turbine from bottom fixed to floating, the rotor is moved closer to the free surface where the effects of shear and surface waves are likely more pronounced. Crucially, a necessary prerequisite to optimizing tidal turbine design in the above contexts will be establishing a detailed understanding of their operational conditions and load characteristics. The importance of such efforts is highlighted by ongoing research in the wind community to better characterize operational wind turbine loading, thought to be responsible for high rates of premature failure in major components, including: main bearings, gearboxes, and generators (Hart et al., 2020; Nejad et al., 2022). It is reasonable to assume that these common failure modes experienced by wind turbines will also manifest in tidal devices, and will be uncovered as more machines are deployed. The shared architectures of wind and tidal turbines therefore presents a unique opportunity to apply the learning from decades of wind turbine research and development to tidal turbines, in order to identify potential issues and then tackle them at this earlier stage of tidal technology development. Beyond the design of individual components, the ability to assess and characterize the sensitivity of tidal turbine rotor load responses is valuable within the decision-making process with respect to both locating and controlling tidal devices. Taking the lead from wind energy research initiatives (Guo and Keller, 2018; Hart et al., 2019; Hart, 2020; Guo et al., 2021; Hart et al., 2022), it is therefore proposed that a first important step in understanding component selection and optimal design, for tidal devices, is establishing a detailed knowledge baseline for the characteristics and drivers of the mechanical loads which enter the system at the turbine hub, before propagating along the drivetrain and ultimately into the support structure. Furthermore, if such work can be undertaken both at scale and through numerical modelling, failure preventative actions may be identified prior to full scale deployment, with the potential for substantial savings to developers. The current paper therefore contributes to these outlined, necessary, research efforts by developing a numerical model for the simulation of tidal turbine rotors in realistic ocean environments. The model is constructed with capacity to advance the complexity of the onset flow into the rotor, and more fundamentally resolve turbulent structures and the turbine's effect on the fluid, compared to hydro-elastic models. The model is presented, validated at tank scale and then applied to study hub-height and wave effects on tidal turbine mechanical loading conditions, characteristics and sensitivities. This is undertaken in the presence of a realistic sheared current and turbulence. The application of this model allows for the analysis of previously unconsidered load characteristics and behaviours, at full scale, for the first time.

Note, for the sake of clarity, tidal rotor locations will be described using "hub height" (above the seabed) throughout, rather than "depth" (below the free surface). This is necessary to ensure that the rotor location is well-defined, since the location of the free surface changes in time.

Section 2 provides an overview of the background to this work, including prior research on the modelling of tidal turbine rotors. Section 3 then outlines the methodology for the current study, including model development and model validation stages. Results and discussions for both model validation and the full-scale analyses are presented in Section 4. Section 5 then concludes the paper.

2. Background

The current section will provide a review of the current literature on tidal turbine rotor loads, with a focus on rotor responses in waves. Included here also, is an outline of the prior learning gained from the wind sector, which provides motivation for the work more broadly.

At this early stage of the tidal industry, developers tend to deploy 'over-engineered' turbines with increased safety factors as mitigation against the uncertainty of operating conditions. By understanding the hydrodynamics better, this uncertainty is reduced, leading to more optimized design and operation, which in turn could help in reducing the levelized cost of energy (LCOE) for the technology and make it a more competitive green energy option in the future. The response to this challenge, both in academia and industry, is typically a combination of numerical modelling and scale physical testing owing to the limited number of turbines in service with data available to analyse. Research is attempting to more accurately characterize hydrodynamic rotor loads, to reproduce the in-service conditions tidal turbines are subject to; namely the often aggressively sheared flows, wave–current interactions and turbulence.

As a starting point, it is useful to define common turbine rotor performance metrics. Rotor performance is generally considered in terms of torque and thrust, Q and, T respectively. In the simplest terms, torque can be considered the 'useful' loading which generates the mechanical rotation from which electrical power is induced, and thrust considered the 'damage' loading that imparts no useful work. These quantities are normalized to give the classical performance indicators C_p and C_T (Eq. (1)) and commonly assessed against the tip speed ratio (Eq. (2)), the non-dimensional rotor speed.

$$C_P = \frac{Q\Omega}{\frac{1}{2}\rho A U^3} \quad ; \quad C_T = \frac{T}{\frac{1}{2}\rho A U^2} \tag{1}$$

$$TSR = \frac{\Omega R}{U} \tag{2}$$

Above, ρ is the fluid density; Ω represents rotor speed; A the rotor swept area; R the rotor radius; and U the normalizing velocity. The performance indicators are sensitive to U, and its computation is non-standardized, so at times it may be more convenient to consider torque and thrust in the absolute. There is a tendency to use both dimensional and non-dimensional quantities interchangeably when describing 'performance'.

Tidal turbine performance is a focus of many experimental campaigns, and research has centred on rotor responses to lab scale flows. Many institutions have designed and manufactured scaled turbines (Allmark et al., 2018; Payne et al., 2017; Gaurier et al., 2015), for the

purpose of tank testing. Facilities open to commercial clients such as IFREMER and FloWave at the University of Edinburgh have examples of generic 3 bladed, horizontal axis devices, which are commonly used. Tank testing has targeted the isolation of key constituents of the real tidal environment and their effects on turbine rotor loads. For example, the effects of turbulence are studied in Mycek et al. (2014), Blackmore et al. (2016), Medina et al. (2017), Gaurier et al. (2020), with Medina et al. (2017) (which tests 2 turbulence regimes) observing correlations between upstream turbulence and rotor performance. Blackmore et al. (2016) shows again the significance of the onset flow field, finding peak power coefficient variations of 10% in the presence of turbulence. Other studies focus on the effects of flow misalignment (Galloway et al., 2014; Martinez et al., 2018), and on rotor responses within tidal arrays (Noble et al., 2020). A unique and important constituent to ocean flows is the presence of surface waves, and experiments have been conducted to assess how waves impact rotor performance (Luznik et al., 2013; de Jesus Henriques et al., 2014; Martinez et al., 2018; Guo et al., 2018; Draycott et al., 2019; Ordonez-Sanchez et al., 2019). It is consistently found that wave impacts on mean performance remain minimal, however the increase in performance fluctuations in the presence of waves is significant (Gaurier et al., 2013; Luznik et al., 2013; de Jesus Henriques et al., 2014; Martinez et al., 2018; Guo et al., 2018; Draycott et al., 2019; Ordonez-Sanchez et al., 2019). For instance, Ordonez-Sanchez et al. (2019) finds that the presence of a regular wave front resulted in an increase in peak loads of 30%, while Draycott et al. (2019) shows peak thrust and power is increased by between 7%–65% and 13%–160% respectively when waves are present. It has also been found that peak loading is proportional to wave height (Ordonez-Sanchez et al., 2019). Lust et al. (2013), Luznik et al. (2013), Guo et al. (2018) also investigate effects from turbine depth in their tow tank experiments. Guo et al. (2018) constructs response amplitude operators for estimating wave loading and shows their sensitivity to submergence; concluding that submergence at 80% of the rotor diameter mitigated the most severe effects of the waves tested.

Complimenting the research undertaken in tanks, numerical models attempt to predict rotor loading computationally. A range of fidelities are present in the literature, from lower fidelity hydro-elastic models implementing a blade element momentum (BEM) approach, to high fidelity full resolution computational fluid dynamics (CFD). Examples in the literature are still fairly limited, so there is a library to fill with new research. Tatum et al. (2016) uses a full resolution approach to simulate a full scale tidal turbine in a single regular wave, implementing both an uncoupled CFD, and a 2-way couple fluid structure interaction (FSI) model. Apsley et al. (2018) however, opts for the actuator-line method when simulating interacting turbines. Others have used the BEM method modified to include wave velocities and added mass forces (Faudot and Dahlhaug, 2012; Guo et al., 2018). There are clear advantages and disadvantages of each model type, BEM methods provide an efficient and fast compute that can provide accurate results in many well-defined flow regimes. They do, however, rely on empirical corrections and statistical models for inflow turbulence. Additionally, rotor effects on the onset flow are only weakly coupled via induction factors, calling into question their validity in application to new flow environments. Higher fidelity CFD methods provide a more fully coupled approach, resolving the whole inertial flow field, and resolving turbulence in a more sophisticated manner, but suffer from high computational expense, especially where full-geometry resolution is simulated. The computational expense may be alleviated, in part, by a move to actuator line representations of the rotor, which apply body forces onto the flow field in place of resolving system geometries. This option represents a middle-ground in model fidelity, allowing for longer simulation times windows while retaining turbine feedback effects on the flow field.

It is the loads transferred from the rotor to the main shaft that researchers in the wind sector are principally interested in when studying loading and failures within the drivetrain. Such research has lead to the optimization of many components across a variety of manufacturers. Subsequently, increases in scale and reliability have followed. An example of this progression is found in the move, by some manufacturers, to direct-drive machines. This removes the gearbox from the drivetrain; a component commonly associated with increased failure rates (Arabian-Hoseynabadi et al., 2010; Carroll et al., 2019; Liu and Zhang, 2020). Another common source of failure is the rotor main bearing, with significant numbers failing earlier than their intended design life; Hart et al. (2019) reports main bearing failure rates of up to 30% over a 20-year design life. Work has been undertaken in this space to investigate main bearing non-steady loading (Hart et al., 2022), progress main bearing modelling (Hart, 2020; Stirling et al., 2021) and explore possible drivers for early failures (Guo et al., 2021). Hart et al. (2019), Hart (2020), Hart et al. (2022) demonstrate that main bearing loading is strongly linked to the characteristics of the onset wind field, having injected aero-elastic model outputs into structural main bearing models. It is a reasonable assumption that the same challenges faced by the wind industry over the past few decades will begin to manifest in tidal devices as more machines are deployed and time-in-service increases. An early step in mitigating the early component failures seen in wind turbines, is via the characterization of the onset flow conditions that drive the loading behaviour. And so, as demonstrated within the wind sector, there is considerable value in model development and load behaviour evaluation for drivetrains in tidal energy devices.

A recent paper by Perez et al. (2022) is the first of its kind to investigate the influence of rotor position within the water column on tidal turbine rotor loading at full-scale. Perez et al. (2022) studies 3 hub heights under a variety of shear currents and wave environments using field velocity data injected into a BEM model, and finds that means and standard deviations of the performance coefficients are more sensitive to shear than to waves in the studied cases. Additionally, it is found that long period waves can double mean performance coefficients, in contrast to others that report negligible increases to torque and thrust signals under wave loading (Ordonez-Sanchez et al., 2019; Guo et al., 2018; Martinez et al., 2018).

3. Methodology

The current paper seeks to contribute to the literature on hub height and wave effects on tidal turbine performance. In addition, we seek to progress the research on the numerical modelling of turbine rotors, by presenting a mid-fidelity model to sit between geometry-resolved CFD and BEM modelling. The model utilizes a CFD-ALM approach to fundamentally resolve the time dependent flow field inclusive of surface waves, a sheared current and turbulence. The benefit of this approach is in the ability to more dynamically effect onset flow conditions, similar to full blade resolution, yet be sufficiently lightweight to allow for longer time-period simulations within reasonable compute times. In effect, this model aims to resolve medium to long term turbine responses with regard to mechanical loads in a complex flow field including surface waves. In this section the methodology is presented for the development, validation and application of this numerical model. The development of the model will briefly outline the model's theory and, as part of the validation, an overview of the utilized experimental data will be given. For validation, the numerical model was configured to represent the University of Edinburgh lab scale turbine. Once validated, the model was adjusted to represent a full scale 1.5MW tidal turbine operating in a realistic ocean environment. A justification for the scale parameters is given, and a novel rotor-load metric is introduced for application in the subsequent analysis. All numerical modelling was undertaken on the University of Edinburgh's high performance computing facility, 'Eddie' (Edinburgh Compute and Data Facility website, 2023).

3.1. Numerical model development

To resolve the multi physics involved in tidal turbine rotor loading, a coupled model is implemented. To study a wider range of conditions, resolving time dependent flows more fundamentally to provide inputs to the turbine model, a mid-fidelity actuator line modelling approach is adopted. The additional complexity of rotor onset flow gained by using a CFD approach coupled with an efficient numerical model of the turbine allows for a larger comparative study as well as a more general model to give confidence in resulting load transfers.

The model is constructed in OpenFOAM-v1912 (Weller et al., 1998) and consists of two key parts; a 3D multiphase domain and an actuator-line model (ALM) embedded within to represent the turbine rotor. Both are more fully outlined in the following subsections. The domain simulates surface waves, shear currents and turbulence, and the turbine effects are projected onto the flow as an additional body force. Both phases (water and air) are solved for using the 3D Reynolds-averaged Navier–Stokes formulation. The discrete layer between the phases is solved for with the volume of fluid (VOF) method. Boundary conditions make use of the olaFlow libraries (Higuera, 2018) and the actuator line model is inputted to the domain using the turbinesFoam libraries (Bachant et al., 2016).

In this study, the general incompressible Navier–Stokes formulation used to solve the coupled system becomes,

$$\frac{\partial \mathbf{U}}{\partial t} + \mathbf{U}\cdot\nabla\mathbf{U} = -\frac{1}{\rho}\nabla p + \nu\nabla^2\mathbf{U} + \mathbf{f}, \tag{3}$$

where $\mathbf{U}$ is the velocity field, ρ the fluid density, p the pressure field, ν the fluid viscosity and $\mathbf{f}$ the additional body force term from the turbine, discussed further in Section 3.1.2. Bold variables denote vector terms.

3.1.1. Multiphase domain solver

The foundation of the numerical model are the Volume-Averaged Reynolds-Averaged Navier–Stokes (VARANS) equations. The VARANS method allows for the simulation of multiple fluids separated by a discrete surface. In the case of this work, as for many other offshore engineering applications, these fluids are water and air. In OpenFOAM®, the "interFoam" solver is used. Assuming the two phases to be incompressible, which is sufficient in this case, the VARANS governing equations (continuity - Eq. (4), and conservation of mass - Eq. (5)) are,

$$\nabla\cdot\boldsymbol{U} = 0 \tag{4}$$

$$\frac{\partial\rho\boldsymbol{U}}{\partial t} + \nabla\cdot(\rho\boldsymbol{U}\boldsymbol{U}) - \nabla\cdot(\mu_{eff}\nabla\boldsymbol{U}) = -\nabla p - \boldsymbol{g}\boldsymbol{x}\nabla\rho + \nabla\boldsymbol{U}\cdot\nabla\mu_{eff} + \sigma\kappa\nabla\alpha, \tag{5}$$

$\boldsymbol{U}$ is velocity; ρ density; p the pressure; $\boldsymbol{g}$ the acceleration due to gravity; $\boldsymbol{x}$ the position vector; σ is the surface tension coefficient; κ the interface curvature; α the volume fraction; and μ_{eff} is the effective dynamic viscosity. μ_{eff} is composed of the fluid's molecular viscosity and a turbulence contribution, such that,

$$\mu_{eff} = \mu + \rho\nu_t, \tag{6}$$

with ν_t the turbulent kinetic viscosity obtained via the user defined turbulence model. The interface curvature term (κ) is defined as,

$$\kappa = -\nabla\cdot\frac{\nabla\alpha}{|\nabla\alpha|}. \tag{7}$$

The key parameter in the above VOF formulation is the volume fraction, α, where $0 \le \alpha \le 1$. An α value of 1 indicates a cell containing only water, while an α value of 0 indicates a cell containing only air. Intermediate values then specify the proportion of each. Fluid properties within each cell are then determined via a VOF weighting function. For example, the density within each cell is given by,

$$\rho = \alpha\rho_{water} + (1-\alpha)\rho_{air}. \tag{8}$$

The current work implemented the interFoam solver through the open-source libraries of olaFlow (Higuera, 2018), developed by Pablo Higuera, and utilized the PIMPLE algorithm. olaFlow provides additional boundary conditions for the generation, absorption and reflection of waves and currents. Turbulence was resolved using an adapted $k-\omega$ SST model (Devolder et al., 2017, 2018; Larsen and Fuhrman, 2018), available through a supplementary olaFlow library. The adapted turbulence model contains an additional buoyancy term that prevents build-up at the free surface.

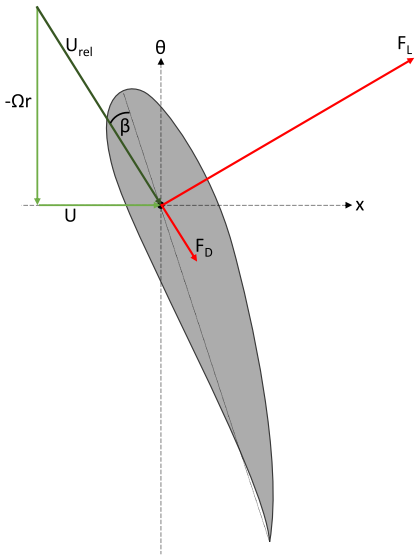

Fig. 1. Diagram of the velocity and force vectors acting on a blade section. Note, the blade section is moving rotationally in the θ axis shown (i.e. upwards).

3.1.2. Actuator line modelling

The ALM formulation used here was originally developed by Troldborg et al. (2007) to model flow around wind turbines. The technique represents turbine blade sections as force distributions, as opposed to via their physical geometry. The model in this work applies the force distribution, $\mathbf{f}$, in Eq. (3). The forces are determined with the use of lift and drag data for the corresponding hydrofoil at each blade section. Lift and drag data at each blade section was generated using XFOIL (Drela, 1989). The implementation of the ALM into this model uses turbinesFoam (Bachant et al., 2016), created by Bachant and Wosnik (2015), Bachant et al. (2018) and validated in Mendoza et al. (2016), Mendoza and Goude (2017, 2020), Onel and Tuncer (2020), Liu et al. (2022). For a more complete introduction to the turbineFoam application the reader is directed to Bachant et al. (2018), here only a brief overview of the theory will be given.

The turbinesFoam ALM is implemented through the fvOptions dictionary, which allows for the simple addition of force terms to the governing flow equation. Fig. 1 illustrates the velocity and force vectors acting at a given blade section. The velocity experienced by the blade section, U_{rel}, is obtained by summing the onset velocity, U, with the velocity as a result of the rotating rotor, $-\Omega r$. The relative direction of this resultant velocity on the section is given by the angle of attack, β. From U_{rel}, the forces of lift and drag, F_L and F_D respectively, are then,

$$F_L = \frac{1}{2}\rho A_{elem} C_l |\boldsymbol{U_{rel}}|^2 \tag{9}$$

$$F_D = \frac{1}{2}\rho A_{elem} C_d |\boldsymbol{U_{rel}}|^2, \tag{10}$$

where A_{elem} is the blade section area (span × chord), and C_l and C_d the lift and drag coefficients for the given hydrofoil, respectively. These coefficients are required as inputs to the model, and are functions of β.

The force calculated here is projected back onto the flow field using a spherical Gaussian distribution, ϕ, where,

$$\phi = \frac{1}{\epsilon^3\pi^{\frac{3}{2}}}\exp\left[-\left(\frac{|\boldsymbol{r}|}{\epsilon}\right)\right]^2. \tag{11}$$

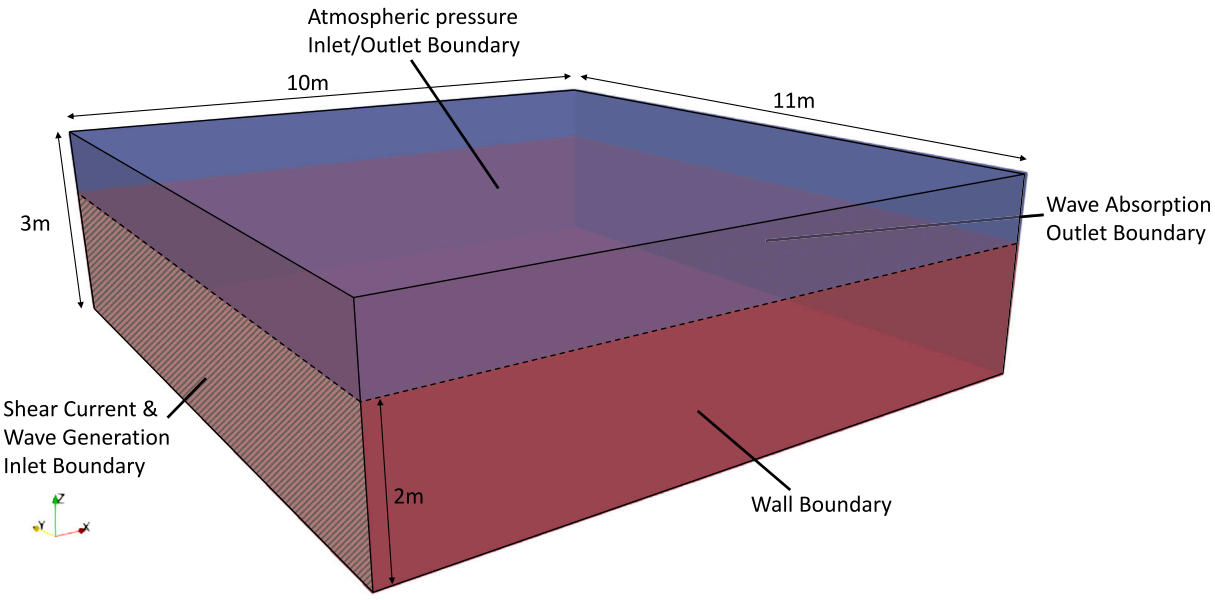

Fig. 2. Computational domain used for the validation cases. Red sections denote water phase and blue air. The hashed section on the inlet boundary denotes the area on which the current profile is applied at time 0s.

ϕ acts on a cell of distance $|\boldsymbol{r}|$ from the actuator line's quarter chord position. To avoid steep gradients and maintain stability, the Gaussian includes the parameter ϵ. ϵ is a width parameter and is set equal to be the maximum of three possible values,

$$\epsilon = \max(\epsilon_{chord},\ \epsilon_{momentum},\ \epsilon_{mesh}). \tag{12}$$

The possible width parameter values are related to: the chord length (l_{chord}) of the element's hydrofoil,

$$\epsilon_{chord} = \frac{1}{4} l_{chord}, \tag{13}$$

the chord length and the local momentum thickness as a result of drag,

$$\epsilon_{momentum} = \frac{1}{2} C_d l_{chord}, \tag{14}$$

and the local cell volume (V_{cell}),

$$\epsilon_{mesh} = 4\sqrt[3]{V_{cell}}. \tag{15}$$

3.2. Numerical model validation

The validation of the numerical model was undertaken in two parts: 1) validation of ALM performance through a range of rotational speeds in the absence of surface waves, and 2) validation of the coupled system in recreating wave loading on the rotor. In this section, data from physical testing at model scale will be introduced, and the methods used to analyse the data against numerical results given.

The model was configured to represent flow conditions in the FloWave wave–current test tank, described below. From Noble et al. (2020), current mapping shows that a plan area of approximately 10 m x 6 m at the centre of the tank – where the scale turbine is located – provides bulk flow conditions that can be considered laterally constant. Because of this, a simple rectangular domain was implemented to maintain computationally cost-effective simulations. The width of the domain was set to 11 m, the length to 10 m, and the height to 3 m to easily accommodate the 2 m water column in addition to the increased water elevations seen when waves are present. Zero-gradient wall boundaries were applied to the bottom and sides of the domain. The side boundaries were sufficiently distanced from the turbine to cause negligible blockage effects. A characteristic 1/15th log-law velocity profile was assigned to the inlet boundary, in line with the physical flow field in the tank (Noble et al., 2015), such that,

$$U(z) = \left[\frac{z}{0.4h}\right]^{\frac{1}{\gamma}} \cdot U_{\infty}, \tag{16}$$

with $\gamma = 15$. In wave validation cases, additional regular wave generation or absorption boundary conditions were added to the inlet or outlet (dependent on whether waves were following or opposing the current). An illustration of the domain is provided in Fig. 2. In all cases, the current boundary condition was kept constant at the reference height velocity used in the experimental data. For the ALM validation, the turbine speed was varied rather than the flow. In all cases, the operation of the numerical model was such that it matched the physical tests as closely as possible.

The numerical turbine model splits each blade into 23 separate blade sections, whose hydrofoil profiles were retrieved from the original design CAD model as 2D coordinates. An estimate of each section's operating conditions was obtained using the following Reynolds number,

$$RE_r = \frac{c(r)\sqrt{U_{rel}^2 + (r\Omega)^2}}{\nu}, \tag{17}$$

where $c(r)$ is the chord length at radius r, Ω is the rotational speed, and ν the kinematic viscosity. This Reynolds number was then used as an input to XFOIL, for calculating the lift and drag properties of each blade section as a function of angle of attack, for each rotor speed simulated. Note, this approximation of lift and drag was done prior to CFD simulations. This constitutes a well-known limitation of such modelling approaches. However, investigation of the effect on the foils' lift and drag properties reveals that a convergence occurs as the Reynolds number increases, reducing sensitivities to these effects at higher TSRs.

3.2.1. Experimental data

The experimental data used to validate the developed numerical model comes from two separate test campaigns. The first was used to validate the ALM, and the second to validate the rotor response to waves. The ALM is validated against the work of Noble et al. (2020), and the wave responses against (Draycott et al., 2019). Both test campaigns were conducted at FloWave, The University of Edinburgh's

Table 1
Summary of validation test case inputs to the numerical model.

Wave height [m]	Wave period [s]	Wave direction	Wave theory	Ref flow speed[a] [m/s]	Turbine speed [RPM]
0.108	1.832	Following	Stokes 1st	0.7755	90.0
0.184	2.498	Following	Stokes 1st	0.7813	90.0
0.0248	3.246	Following	Stokes 1st	0.7823	90.0
0.0446	3.242	Opposing	Stokes 1st	0.7678	90.0
0.198	2.497	Opposing	Stokes 2nd	0.7900	90.0
0.361	3.242	Opposing	Stokes 2nd	0.8112	90.0

[a] This is the reference velocity for the log law profile, in this case taken at z = 1.4 m to match physical testing.

combined wave and current test tank. The FloWave test tank is a circular combined wave and current tank of diameter 25 m. It comprises 168 active-absorbing wave paddles situated around its circumference to generate and absorb surface waves, and a circular arrangement of 28 impellers located beneath the tank floor to generate currents. With this configuration, FloWave can generate independent waves and currents about 360 degrees.

The University of Edinburgh tidal turbine is a lab scale turbine designed to be bottom fixed and consisting of 3 fixed-pitch blades, with a rotor diameter of 1.2 m. The turbine is driven by an AC motor and was designed to operate at constant speed. The blades are constructed of aluminium and make use of the common NACA 63-8XX series hydrofoil profiles. The turbine has been used in many test campaigns to date. For a detailed introduction to the turbine's design and manufacture, the reader is pointed to Payne et al. (2017). The data obtained from the campaigns included rotor torque, thrust and angular velocity, in addition to flow velocity point measurements captured using FloWave's acoustic Doppler velocimeter (ADV). Flow measurements in Noble et al. (2020), important to part 1 of the model validation (ALM validation over a range of speeds), were taken at hub height 2 rotor diameters upstream of the operating turbine. These measurements were not synchronous with the turbine load measurements. Additionally, in Draycott et al. (2019), wave elevation was captured directly above the rotor plane.

3.2.2. Actuator line turbine validation

The ALM was validated across 7 TSRs, from 1 to 7, to identify its capability to correctly reproduce blade loads in terms of thrust and torque over a range of rotor speeds. The numerical and physical turbines' tip speeds were normalized using the hub height velocity, taken 2 rotor diameters upstream of the rotor. The TSR was altered for each case by setting the turbine's rotational speed. The onset flow remained constant throughout, during both physical testing and numerical modelling. Additionally, simulations were performed using a standard BEM code – NREL's AeroDyn – to identify the CFD model's capabilities when compared to a lower order numerical approach. The classical non-dimensionalized performance coefficients, C_P and C_T (Eq. (1)), were used as the metrics for validation.

3.2.3. Wave validation

For validating the wave loading response of the model, the turbine was kept at a constant TSR; the turbine speed and current inputs remained constant at approximately 90 RPM and a nominal 0.81 m/s respectively. In the experimental testing, a velocity signal was taken 600 mm below the mean water line and so the mean velocity from the signal and the reference height (z=1.4 m) was used to identify a suitable shear profile for use in the numerical model (Eq. (16)). Three regular waves were then applied in two directions – following and opposing the current – such that six simulations were performed in total. Table 1, summarizes the wave heights and frequencies considered in these test cases.

3.3. Model upscaling and full scale simulations

In order to investigate realistic hub loading in a representative real-world ocean environment, the validated test model was upscaled to represent a full-scale tidal turbine. The upscaled model was parameterized to represent a 1.5MW machine, situated in a realistic tidal flow site. To ensure the setup was typical of a real tidal site, inputs were based on the MeyGen site in the Pentland Firth. Coles et al. (2018) provides an excellent resource for the characterization of the MeyGen site. Matching profile information from Coles et al. (2018), the input sheared flow was set to 3 m/s at 20 m, the vertically extrapolated using a 1/7th power law. This profile shape is considered a good representation of reality in that it is consistent with the findings of Coles et al. (2018) and is equally confirmed by Lewis et al. (2017), who investigated a similar tidal site in the Irish Sea. Wave heights and periods recorded in Coles et al. (2018) range from 1.27 m to 4.89 m, and 5.39s to 11.48s respectively. A turbulent length-scale of 50 m was also shown to be reasonable in a 3 m/s current.

The domain width was set to 110 m such that wall boundaries at each side would not affect the turbine response. The water depth was specified as 50 m, again representative of the MeyGen site. The streamwise dimension was set to 100 m to ensure the turbine – positioned at the centre of the domain – experiences fully developed flow, with no effects of back pressure from the outlet boundary. In terms of the numerical turbine, no full-scale geometric information was available with which to accurately model an in-service tidal turbine. The full-scale numerical turbine was therefore specified via linear (1:15) scaling of the laboratory device. The previous 23 blade sections remain, with scaling applied to the chord lengths, rotor diameter and hub diameter. In the upscaled model, the rotor diameter is 18 m and the hub diameter is 1.8 m. For full-scale simulations, the turbine speed was set to a constant value of 14 RPM. Full-scale turbine TSR values were all in the range $4 \leq \text{TSR} \leq 5$, corresponding to the region of good model performance shown in validation results, see Section 4.1.1. While real tidal turbines of this size may not conform exactly to the resulting scaled model, as outlined in Section 1, the purpose of the current study is to better understand the load conditions, characteristics and sensitivities of full-scale tidal devices. Since the qualitative and relative load responses of the upscaled model, under the considered conditions, would be expected to be similar to that of in-service turbines of the same size, the developed model is deemed sufficient for the purposes of this analysis.

A program of simulations was undertaken using the full scale setup, wherein, simulations were performed in a sheared bulk flow for a range of wave and rotor height combinations. A full description of the regular waves used in the simulations is found in Table 2. For each wave in the table, a simulation was run with the rotor position (hub height) set to 15, 25 and 35 m above the sea bed. All waves were simulated as following the current; additionally, the three 11.5s period waves were also simulated opposing the current. The shorter period waves could not be simulated opposing the current due to wave blocking effects. Confidence in the results from such complex wave–current interactions would be questionable while relying on only a simple superposition approach. Additional control simulations were performed at each hub height in the absence of waves. This resulted in an overall

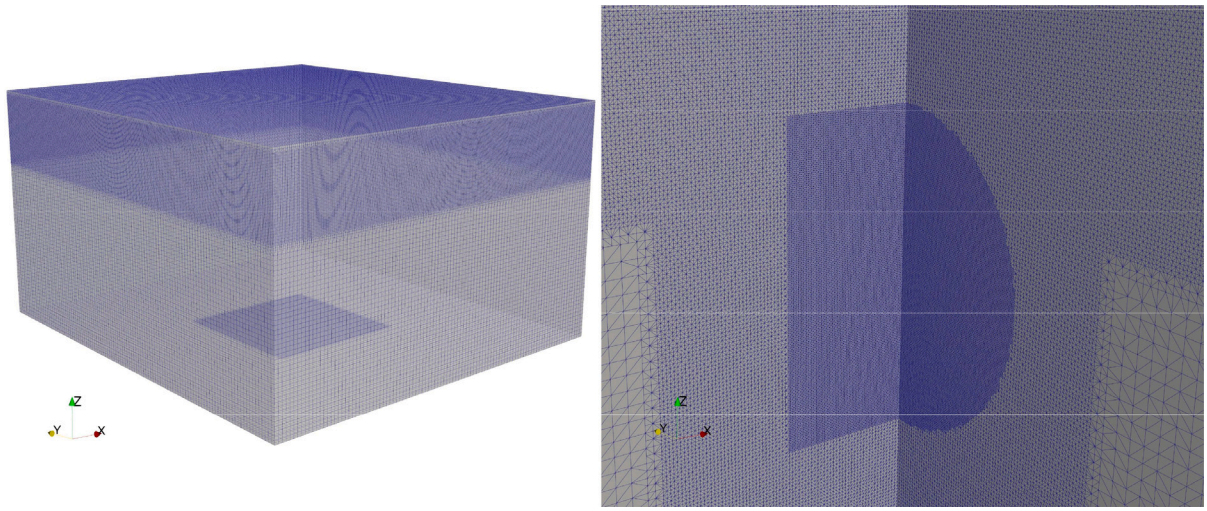

Fig. 3. Example of a mesh used from a 35 m hub height case simulation, highlighting the refinement regions around the turbine and at the free surface.

Table 2
Regular waves used in the full scale simulations.

Wave height [m]	Wave period [s]	Wave length [m]	Wave steepness (H/L)	Water category (d/L)	Wave theory
1	5.5	47.2	0.021	Deep	Stokes 2nd
3	5.5	47.2	0.064	Deep	Stokes 2nd
5	5.5	47.2	0.106	Deep	Stokes 3rd
1	8.5	112.0	0.009	Intermediate	Stokes 2nd
3	8.5	112.0	0.027	Intermediate	Stokes 2nd
5	8.5	112.0	0.045	Intermediate	Stokes 2nd
1	11.5	191.5	0.005	Intermediate	Stokes 1st
3	11.5	191.5	0.016	Intermediate	Stokes 2nd
5	11.5	191.5	0.026	Intermediate	Stokes 2nd

programme of 39 simulations in total. Mesh independence for the full scale simulations was achieved at approximately 10-million cells. A mesh example is available in Fig. 3, where mesh refinement regions can be seen at both the free surface and rotor location. Simulation lengths of 40s were prescribed, allowing for sufficient data collection beyond the settling of numerical transients in all wave cases.

3.3.1. Maximum load span (MLS)

In addition to the standard rotor-load quantities of torque and trust, later analysis of results warranted defining a suitable metric for quantifying observed characteristics in the out-of-plane rotor moment loading patterns (see Section 4.2.2). Focus was placed on the out-of-plane rotor moments due to their importance in the context of drivetrain and structural loading. The constructed out-of-plane moment metric is the *maximum load span* (MLS), which seeks to capture the magnitude and principal direction of moment load variations seen within each simulation. The resultant out-of-plane rotor moment magnitude (R), given the coordinate system illustrated in Fig. 4 (right), is given by,

$$R = \sqrt{M_y^2 + M_z^2}. \tag{18}$$

On construction of a polar plot representing the resultant out-of-plane rotor moment variations in time, for instance see Fig. 10(a), the reader will notice the cyclic nature of the data plotted. Each data-point in the resulting trace is represented by a magnitude and angle. The MLS identifies the data points on the traces separated by the greatest distance on the polar. The adjoining line between these points then becomes the MLS, which (referring to Fig. 4) has *magnitude* (d),

$$d = \sqrt{r_1^2 + r_2^2 - 2r_1 r_1 \cos(\theta_2 - \theta_1)}, \tag{19}$$

and *principal direction* (ψ),

$$\psi = \theta_1 - \sin^{-1}\left(\frac{r_2 \sin^{-1}(\theta_2 - \theta_1)}{d}\right). \tag{20}$$

While certainly a rudimentary metric, the MLS captures two key characteristics present in the moment loading patterns considered in this work. As such, it allows for features present across all results cases to be readily summarized and compared.

4. Results & discussion

This section will present and discuss the findings of this work in two parts. The first will focus on the validation results for the constructed model, in terms of simulating the system from both a turbine, and wave–current perspective. The second part will analyse the results of the full scale turbine study.

4.1. Numerical model validation

4.1.1. Actuator line turbine validation

As has been described, the ALM was simulated over a range of TSRs, and key performance indicators – C_P and C_T – were obtained. The performance indicators serve as a benchmark for validating the model against experimental data. An indicative set of values were also obtained from AeroDyn (NREL's BEM solver module in OpenFAST) simulations, using inputs consistent with the CFD model, as additional confirmation of model validity.

The results for all data sets are shown in Fig. 5. In the figure, the pink markers and error bars indicate the experimental data. The error bars illustrate the maximum and minimum attainable values of C_P and C_T, using one standard deviation, of the torque, thrust, rotational speed, and velocity signals.

The general observation from both plots, in Fig. 5, is that the CFD model and experimental data are in reasonable agreement throughout the range of TSRs. Indeed, both numerical approaches return performance indicator results which fall within the error bounds of the

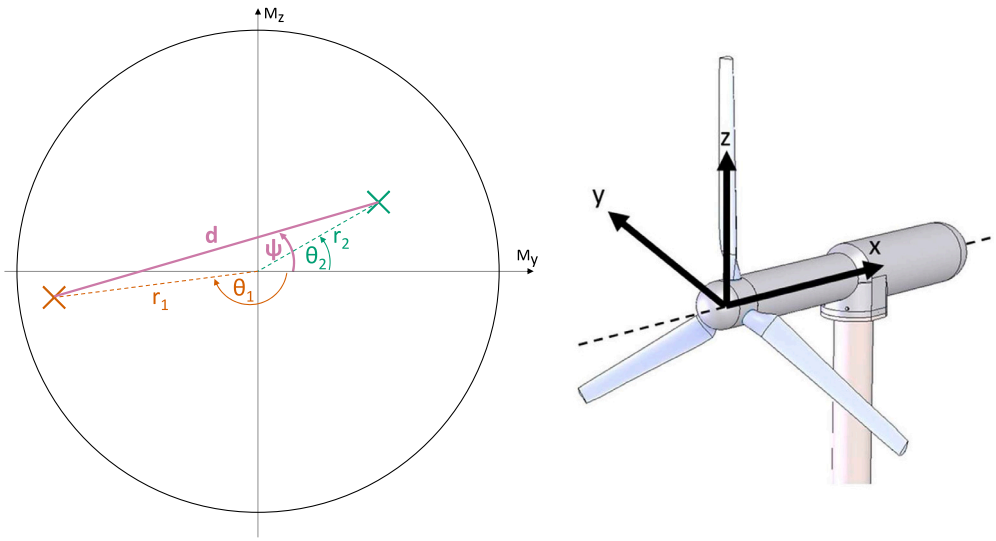

Fig. 4. (left) Maximum load span definition, illustrating the MLS between the 2 points determined as maximum distance from each other on the polar plot. d representing the magnitude of the MLS and ψ the angle at which it acts. (right) Definition of the coordinate system used in the analysis of rotor load, such that a moment about the y-axis (M_y) is pitching of the rotor and a moment about the z-axis (M_z) is yawing. Positive directions are in accordance with the right-hand-rule.

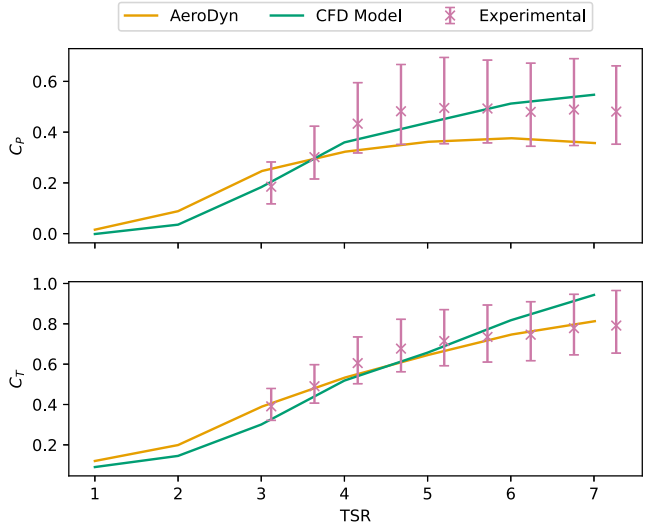

Fig. 5. Plots of C_P (top) and C_T (bottom) showing the outputs from the CFD model, the AeroDyn model, and the experimental data. Error bars on the experimental data indicate the minimum and maximum achievable values based on one standard deviation in the velocity, torque, thrust and rotational speed signals.

experimental data. Recognizing here that the scope of this part is to validate the CFD model in a low complexity flow, and not to compare model performance with a BEM approach, the BEM model is included as an additional check. That being said, the CFD model is arguably in better agreement with experimental data in regard to C_P, though this is less clear regarding C_T. Based on these results, the performance of the two modelling approaches (BEM and CFD) appear comparable. However, this is only in the context of time-averaged performance coefficients, and not necessarily indicative of the quality of the predicted time-varying load response behaviour of each model. CFD modelling was used in the current study since it is able to more fundamentally resolve non-steady inertial flow effects and fluid–structure interactions.

Considering the CFD model outputs versus the experimental data, a divergence is evident, beyond a TSR of 6, for the CFD model C_T values. This is indicative of an over-production of rotor thrust beyond a certain rotor speed in the numerical model. This may be due to a disparity between physical fluid–structure interactions of the real turbine, and the representation of these interactions in the 2D XFOIL code, used to obtain lift and drag data. For instance, due to the relatively high rotational speed of the physical turbine, it is quite possible that a complex 3D flow develops around the blade, including flow separation. Such effects cannot be adequately resolved using a panel method. In the absence of available experimental data for the given blade sections, a more complex CFD approach could be used to try and improve the sectional lift and drag data for the hydrofoil sections. However, this would come with a significant increase in complexity and computational cost. For the purposes of this work, the model can be seen to achieve an adequate reproduction of realistic turbine performance. In particular, very good agreement to experimental data is seen for the mid-range TSR values which are associated with rated operation.

4.1.2. Wave validation

To validate the wave–current boundary conditions and their effect on rotor response, a series of simulations were conducted with the numerical turbine model operating at constant speed. Six cases in total were run, with time series of rotor torque, thrust and wave height compared to those in the experimental data. Two example sets of results are provided in Fig. 6, where one contains following waves and the other contains opposing waves.

In Fig. 6, good agreement may be seen for all signals regarding the frequency content. The CFD model torque signals may be seen to track the upper bounds of the experimental data in both the following and opposing waves. The thrust signals, on the other hand, show a clear over-prediction from the CFD model. The likely reason for this behaviour was discussed in the previous section. The CFD model was simulated with the turbine operating at a TSR of 7, to match that of the experimental turbine. Fig. 5 showed a slight deviation from experimental data in C_P, and further deviation in C_T at this operating point, these observed results are therefore expected based on that prior analysis.

A further observation which can be made relates to the phasing of the data types, with the CFD rotor torque and thrust seemingly phase-shifted from the experimental data. The signals from each data type are fully synchronized with their type. To synchronize the data types with each other, wave height was chosen as the control parameter. Having done this, the experimental torque and thrust signals tend to lag behind the numerical results. There are a few potential explanations for

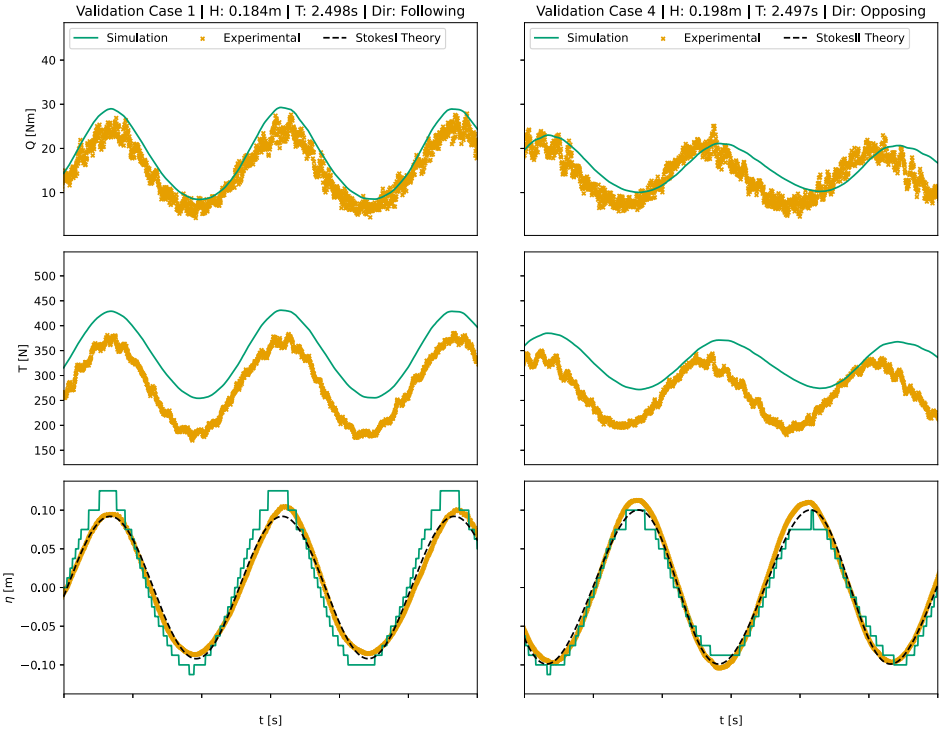

Fig. 6. Wave case validation signals from validation case 1 (left) and validation case 4 (right). Experimental data indicated by the orange and simulation data is the green traces. A black dashed trace in the wave elevation plots represents the theoretical wave elevation from the Stokes theory used.

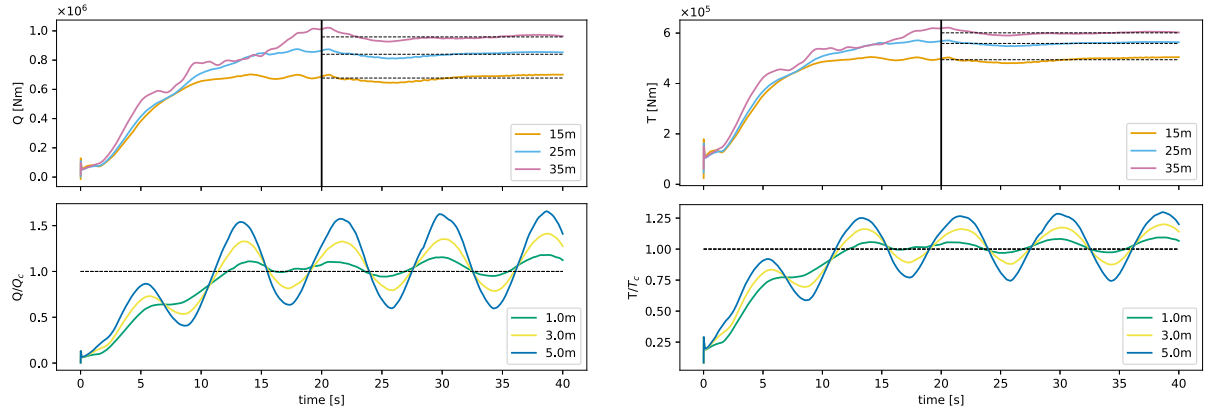

(a) Torque (b) Thrust

Fig. 7. Time series of the turbine torque/thrust (top) from the control simulations (i.e. those with no waves), the vertical line at 20 s indicating the point at which steady state is entered and transients have settled. The bottom plot shows time series' of normalized torque/thrust response in 3 sample wave heights. The cases are following waves at a period of 8.5 s and a distance from the sea floor of 25 m.

this behaviour 1) is that the wave gauge position in the experimental work may have been slightly off the rotor plane position, or 2) there may be more complex wave–current interactions at play which are not captured in the CFD modelling. Since the observed phase-shift is small, it is of little consequence to the investigations undertaken in this work.

The CFD boundary conditions are those available in olaFlow (Higuera, 2018) and these have already been validated independently in other works. In the current work the wave elevation, η, comparisons (Fig. 6) therefore mainly serve to validate the setup of the presented model. The corresponding theoretical trace has also been plotted (black dashed line) for convenience. In general, all three data types match well to the experimental data in both following and opposing wave cases. Note, the CFD elevation data is castellated due to the method used to track the free surface, which simply identifies the cell where α quantity (see Section 3.1.1) is closest to 0.5. This method provides adequate verification that the wave conditions are as expected. The slight wave amplitude variations, versus their theoretical counterpart, is also due to the same surface tracking method. Hence, this disparity does not impact the turbine outputs.

In summary, it has been shown that the CFD model agrees well with experimental data, across analysed cases, in terms of both rotor torque and thrust responses respectively. A small offset in the magnitude of thrust response was observed to occur beyond a TSR of about 6. However, as described in Section 3.3, full-scale simulations were undertaken for turbine TSR values in the range $4 \leq \text{TSR} \leq 5$ where close agreement with experimental results has been demonstrated. The numerical model

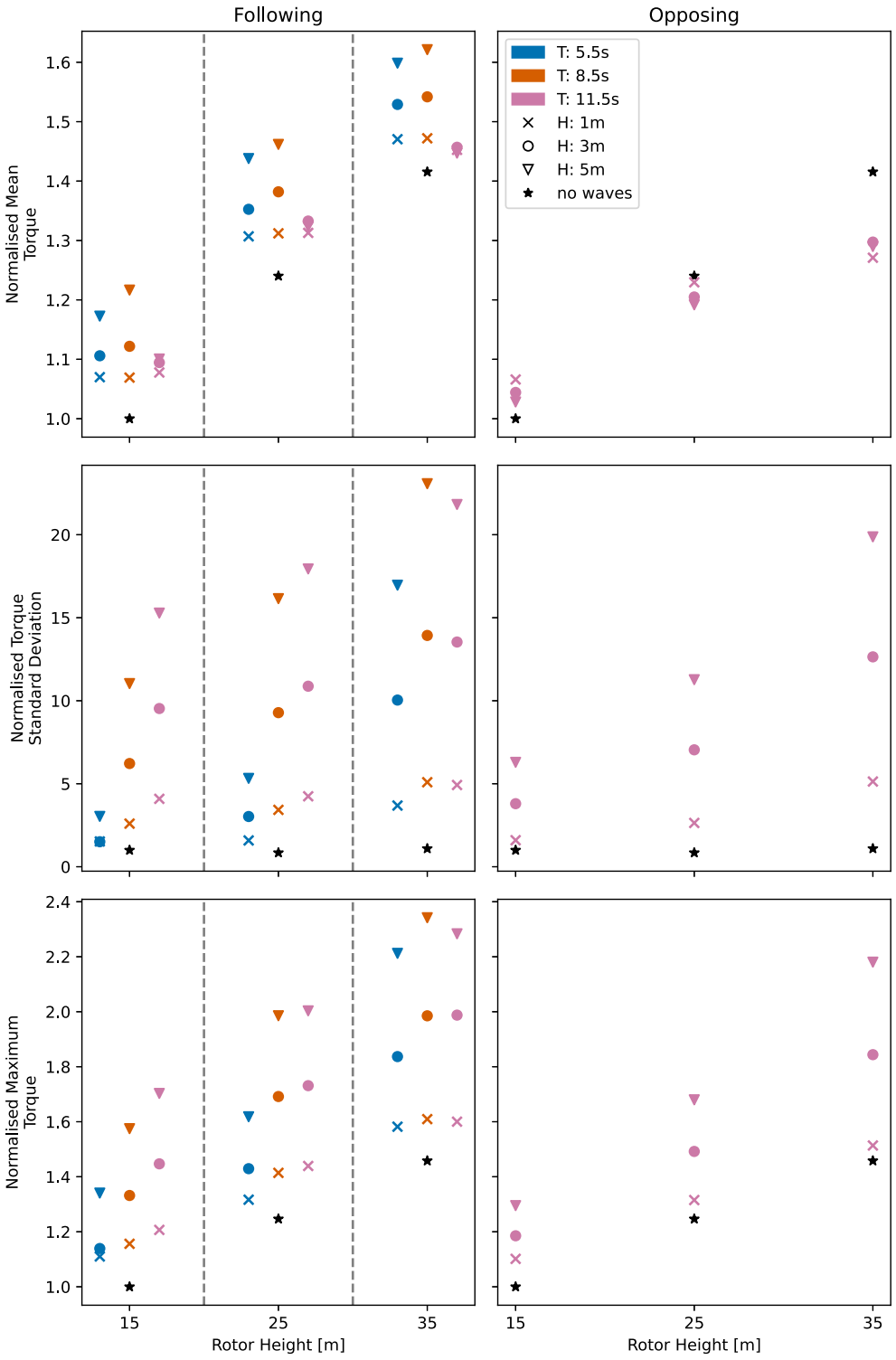

Fig. 8. Rotor torque statistical scatter plots for all simulated cases.

is therefore considered to have been successfully validated within the scope of this analysis.

4.2. Full-scale simulation results

This section will now present and discuss the results of the full-scale simulation study. First, the rotor torque and thrust responses are considered, this forms a basis for onward examinations of the data. With regard to the no-wave 'control' cases, the torque and thrust signals for the 1.5 MW turbine located at each of the three rotor heights are shown in Fig. 7 (top). The orange, blue and pink traces correspond to the rotor at 15 m, 25 m and 35 m respectively. In these plots, a numerical transient settling time of around 20 s, indicated by the vertical black line, can be observed. During all subsequent analyses, this first 20 s of data is removed in order to focus on the steady-state behaviour attained after this point. The steady-state region shows that, as might be expected in a shear flow, rotor torque and thrust increases with rotor height, owing to greater current speeds higher in the water

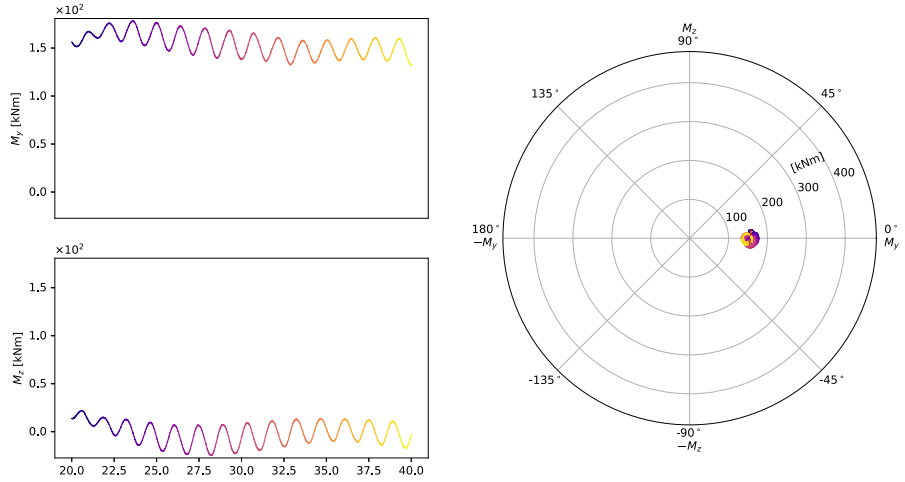

Fig. 9. Out of plane rotor moment plots taken from the control no-wave case with a rotor height of 15 m. Case is plotted in Cartesian (left) and polar (right), which are colour mapped such that the polar projection can be traced through time.

column. The mean values of the signals in the steady-state region are indicated by horizontal dashed lines. The magnitudes of these values are specific to this hypothetical turbine, so conclusions should not be drawn based on their absolute value. Instead, we are interested in the relative behaviour when compared to later presented wave cases.

Moving now to cases in which surface waves are present, Fig. 7 (bottom) shows a subset of torque and thrust signals at different wave heights. These results are all from the 8.5s period following-wave cases, at a rotor height of 25 m. They are each normalized using the corresponding mean value from Fig. 7(a) (top), at the same rotor height. The figure shows all three wave heights, with the amplitude of the oscillating signals seen to increase as the wave height increases. This behaviour is consistent with the results of Ordonez-Sanchez et al. (2019), Draycott et al. (2019), which highlight the increased variance observed in rotor response signals in the presence of waves in physical model testing. Returning to the results in Fig. 7(a), the peak torque loads may be seen to increase by 25%, relative to the no-wave case, for the 5.0 m wave. This confirms that experimentally observed increases in peak loading of up to 30% (Ordonez-Sanchez et al., 2019), seen in scaled tank tests, also occur at full-scale.

4.2.1. Rotor loading summary statistics

Summary statistics across the complete set of full-scale simulations are now considered. First, rotor torque statistics, in terms of means, standard deviations and maximum values, are considered. Fig. 8 shows these torque statistics, normalized using the 15 m hub-height control case. As would be expected, the no-wave control cases show an increasing trend with rotor height. Considering the *following wave* cases of mean rotor torque results (top left of the figure), a clear trend is present of an increasing mean torque with hub height. This is readily interpreted as the effect of an increasing mean velocity for flow higher in the water column. Increases in wave height also result in an increased mean rotor torque in most cases. The exceptions to this are the 11.5s wave period cases, where any sensitivity to wave height appears to have vanished. The mean torque in such cases is clustered close to the 1 m wave results at other wave periods. What is occurring here demonstrates the complexity and interdependence of the multifaceted system being modelled. In more detail: wave impacts on the bulk flow are increased with increasing wave period, due to the increased energy in longer waves. While it is tempting to interpreted this as solely adding kinetic energy to the overall flow in the form of an increased downstream velocity (resulting in a greater mean rotor torque), this is not the case. The form of wave orbitals, which distort flow velocities and directions, occurring in longer period waves introduce misalignment between the flow and the turbine's plane of rotation. As the wave length increases, so does the depth to which the wave orbitals propagate, with the above effects therefore experienced across a greater proportion of the rotor. This, coupled with the wave orbitals becoming wider (horizontally) and shorter (vertically) as the water-depth becomes categorized as intermediate, drive non-negligible changes in onset flow angles. For example, quantitative analysis of these effects in the 35 m hub height (5 m wave) case revealed that the average onset flow angle at two rotor diameters upstream of the rotor-plane changed from −2.23° in the 8.5s period case to 1.33° in the 11.5s period case. This resulted in mean angles of attack (averaged over one blade throughout the 20 s simulation window) of 19.85° and 18.09°, respectively. This serves to highlight that relatively minor changes in the angle of the onset flow can result in significant impacts to the mean rotor torque. Attention is now turned to the *opposing wave* cases (top right of the figure). Interestingly, there is only a small sensitivity to the presence of waves at hub heights of 15 m and 25 m. A significant reduction in the mean rotor torque then occurs at a hub height of 35 m when waves are present. This is again a result of complex flow interactions, similar to those described above. Also of note is the fact that the mean rotor torque was found to be relatively insensitive to wave height for opposing waves cases at all hub heights.

Contrary to other studies that find minimal effects of waves on mean performance (Ordonez-Sanchez et al., 2019; Guo et al., 2018; Martinez et al., 2018), these results indicate that the presence of waves can have a non-negligible effect on the mean rotor torque. For instance, the 8.5s period following waves show the greatest increase in mean torque against the no wave case. At a rotor height of 25 m, this increase is in the range of 7.18% to 22.15% from the lowest to highest wave height, respectively. Equally, in the opposing cases, mean torque was shown to reduce significantly at the highest rotor position, with a reduction of 14.46% relative to the no wave case. Where the presented results are in agreement with other works in the literature is with respect to increasing fluctuations in the presence of waves. This may clearly be seen in the standard deviation results of Fig. 8 (middle), which show significant increases in rotor torque standard deviations in the presence of waves. While the no-wave cases show little change in terms of signal standard deviations as the rotor moves closer to the free-surface, at the 35 m rotor height (5 m, 8.5s waves) standard deviations increase by in excess of 2500% compared to the control case. This represents a considerable change to the rotor loading and, in turn, the load fluctuations entering the drivetrain. A further find here are the observed increases in torque standard deviation with wave period. Both the 15 m and 25 m rotor heights show a consistently increasing value of standard deviation with wave period. At the 35 m rotor height, however, the peak standard deviation occurs at the 8.5s wave period

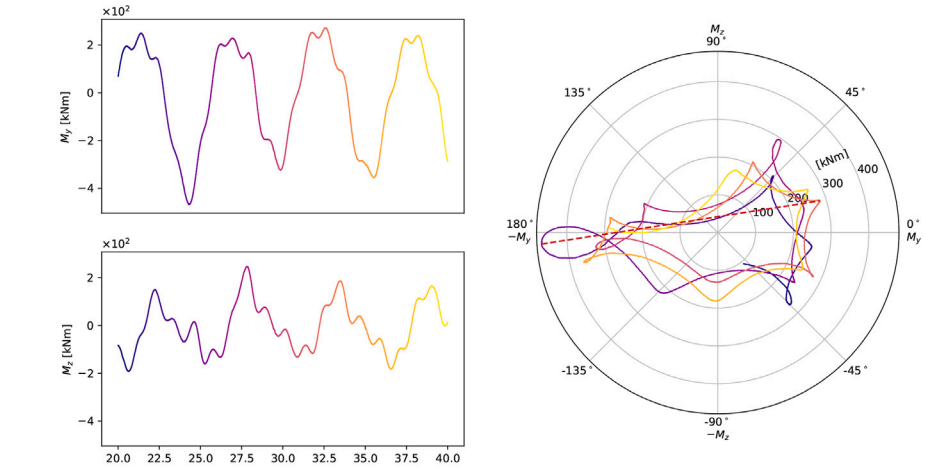

(a) wave period: 5.5s

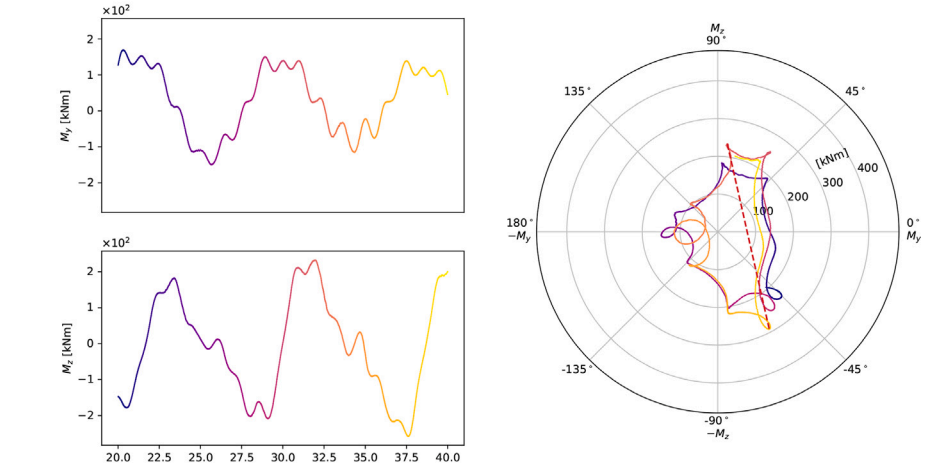

(b) wave period: 8.5s

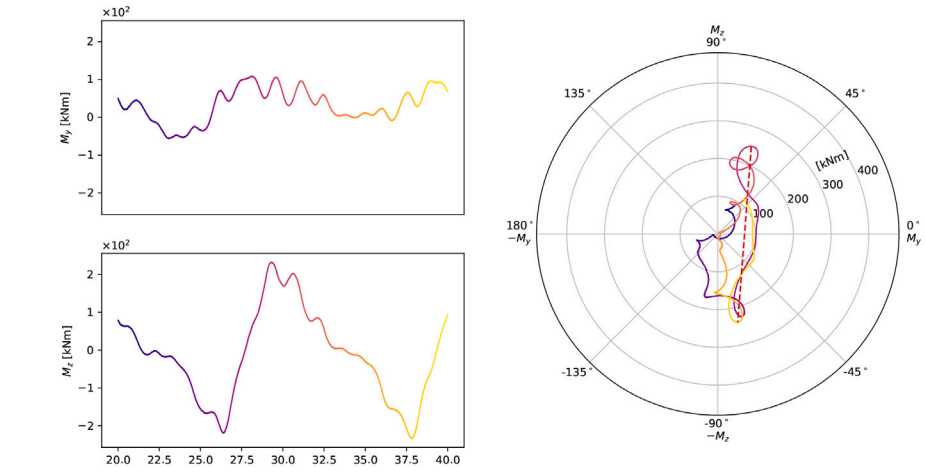

(c) wave period: 11.5s

Fig. 10. Out of plane rotor moment plots taken from 35 m hub height, 5 m wave height, following wave cases. Cases are plotted in Cartesian (left) and polar (right), which are colour mapped such that the polar projection can be traced through time.

before falling slightly again at the 11.5s period. This likely relates to the complex flow effects described previously. Finally, the maximum rotor torque results of Fig. 8 (bottom) are considered. Many of the same trends are again observed the maximum torque responses. As would be expected, an increase in rotor and/or wave height results in increased maximum torque values. A trend of increasing maximum torque with increasing wave period is also observable up to a rotor height of 35 m, at which point an increase in wave period from 8.5s to 11.5 leads to a small reduction in maximum response. As previously, this results from complex flow effects. More generally, the presence of waves can be seen to increase peak rotor torque values by up to 80% (relative to no waves). Similarly, an increase in rotor height of 10 m is predicted to increase the maximum rotor torque by around 20%, for the conditions simulated in this work.

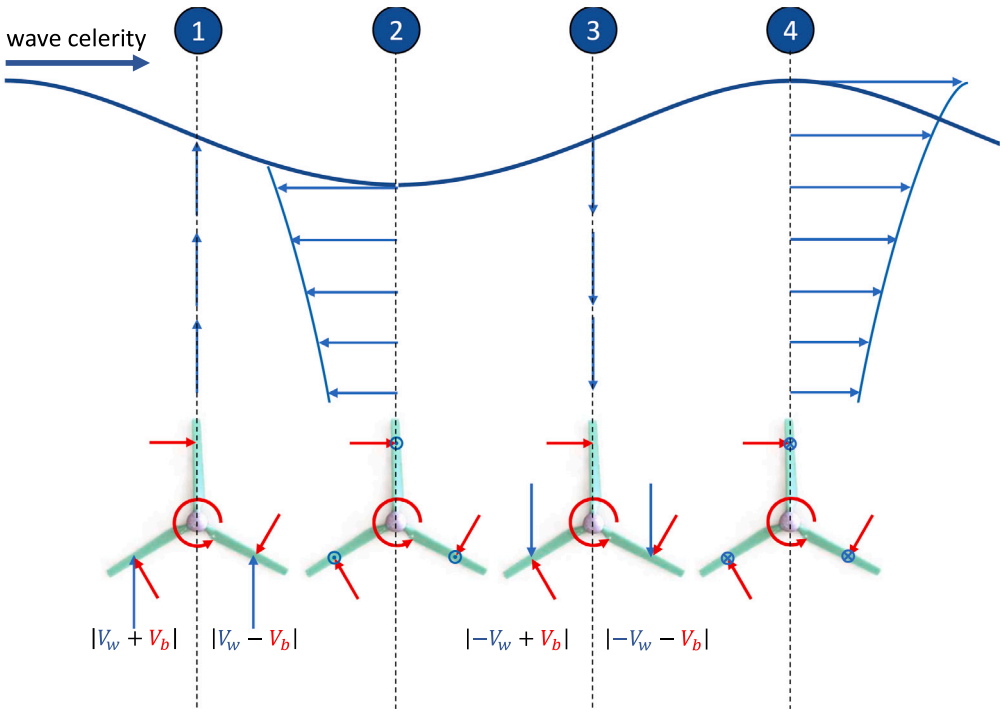

Fig. 11. Illustration of how wave induced velocities could cause asymmetric thrusting over a rotor. Blue vectors indicate wave velocities and red apparent velocities due to the turbine's rotation. The rotors have been rotated to visualize, but in this example would be normal to the wave celerity.

Many of the same results trends, and additional influences from complex flow effects, are evident in rotor thrust results (see Fig. 13 in Appendix). In particular, for thrust results also, the longest period wave induces a notable drop on the mean thrust value, while thrust standard deviations and maximum values remain relatively unchanged.

Perhaps the most important finding in the presented results is the impact of longer period waves on rotor torque and thrust. Crucially, these results indicate that long period waves may lead to a tidal device experiencing what is arguably the "worst of all worlds", where induced flow misalignments drive a reduction in the mean torque (so a reduction in available energy) while, at the same time, the damaging fluctuations and maximal loads in thrust and torque remain relatively unchanged. Hence, under some 'normal' conditions in which a subset of full-scale tidal turbines operate, complex flow interactions may be occurring that result in the turbine experiencing both low energy capture and high levels of 'damage'.

4.2.2. Non-steady hub loading

The study of non-steady rotor loading in this work is focused on the out-of-plane resultant rotor moments, which represent key input loads to the drivetrain system. Fig. 9 shows out-of-plane rotor moment results, as both Cartesian component time-series and as a polar trace, for 15 m hub height results in the absence of waves. Without the presence of wave, only relatively small cycles are present in the resultant moment, which is centred on the M_y axis. This indicates that the rotor is, on average, overturning in pitch. This pitching moment is consistent with the higher flow velocities at the top of the rotor, present in a sheared tidal flow.

Fig. 10 then shows the same results when the turbine is at a hub height of 35 m and exposed to 5 m following waves of various periods. In this latter figure, a markedly more complex loading pattern is observed. Considering the Cartesian time series of M_y and M_z, a comment can be made on the frequencies present in the signals. Firstly, the wave frequency is clearly reflected in each set of results. On closer inspection, some evidence of the blade passing frequency (3P) is recognizable in the smaller fluctuations. Owing to the rotor speed, of 0.233 Hz, a blade pass should fall at intervals of around 1.43s. This is certainly the case in Fig. 9 in the absence of waves, however, it is not fully born out in Fig. 10. This is again due to the complexity and interdependency of various flow field effects in the presence of waves, and associated interactions with the turbine blades as they pass through the flow. The inclusion of waves can be seen to introduce cyclical trajectories in the resultant rotor moment polar traces, similar to those which have been studied previously in the context of wind turbines (Hart, 2020; Hart et al., 2022). Of particular note is the fact that the form these cyclical out-of-plane moment trajectories take is dependent on the wave period. Considering the moment trajectories taken in turn from the shortest wave period (Fig. 10(a)) to the longest (Fig. 10(c)) notice that the moment cycles progress from being largely pitch-dominated to yaw-dominated. The observed dependence on wave period is partially explained by the propagation of wave velocities through the water column. Longer waves impart larger orbital velocity structures to greater depths. From linear wave theory, to depths of half a wavelength in deep waters and to the seabed in intermediate or shallow waters. If these wave orbitals scale to the order of a tidal rotor plane, the flow is significantly adjusted between the top and bottom of the rotor, respectively. In effect this will amplify the pitch moment response present as a result of a sheared current alone. The cyclical nature of wave imparted velocities varies the apparent velocity at the rotor top and bottom, leading, in turn, to cycling between positive and negative pitching moments. The observed transition from pitch dominant cycling to yaw dominant cycling, however, requires a more in-depth consideration. Note, the rotational frequency of the turbine is 0.233 Hz, which corresponds to a blade passing frequency of 0.7 Hz and a TSR of 4.4. Therefore, all modelled waves are quasi-steady from the perspective of the rotor. This indicates that these results are not due to any sort of fortunate combination of rotor/blade and wave phasing. To explore what *is* driving the observed behaviour, Fig. 11 is included to aid the following discussion. What is likely occuring as the wave period increases is that there is a greater prevalence of vertical velocities induced by the wave, owing to the increased levels of energy in the wave at large periods. These vertical components have an opposite effect on the apparent flow velocity experienced by blades on either side of the central streamwise plane, due to the directionality of the

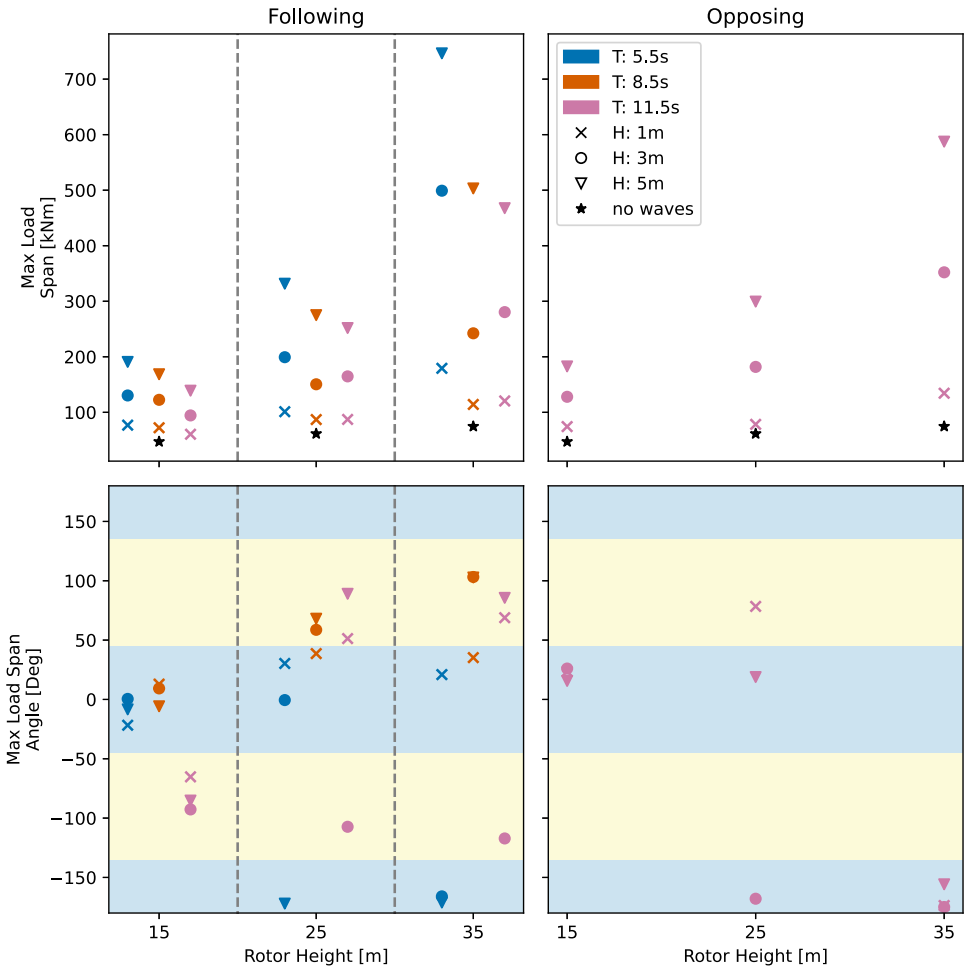

Fig. 12. Scatter plots showing the MLS magnitude (top) and direction (bottom) for all simulation cases; both following (left) and opposing (right) waves. The blue shaded regions on the angle plots indicate rotor pitching load dominance and the yellow regions indicate rotor yawing load dominance.

turbine's rotation. Due to such effects, the thrust distribution across the rotor becomes asymmetric, leading to a change in the turbine yawing moments, and similarly there will be influences on the turbine pitching moments. In the cases presented here, this yawing effect becomes the dominant load behaviour for the longest wave period. This, in turn, indicates that the wave-generated vertical velocity perturbations are large enough to overcome the horizontal velocity under these operating conditions. The studied turbine was therefore found to be subject to what will be referred to as "**wave-driven moment-type dominance**".

The MLS is also shown in each of the plots in Fig. 10, from which it is clear that the magnitude and direction provided by this metric allow for the principal features in each to be readily described in numerical form. Time varying out-of-plane rotor moment behaviour is therefore examined across all simulation cases via the MLS metric. Fig. 12 contains the MLS magnitude and principal direction results. In the absence of waves, a small but steady increase in MLS magnitude is present with rotor height. In the presence of waves, however, it is clear that there is a strong correlation between increased MLS magnitudes and increases in rotor height and/or wave height. Also clear in these results is a consistent reduction in MLS magnitude with wave period. Therefore, higher MLS values seem to correspond to a combination of large wave heights and small wave periods. This suggests that an increasing wave frequency is tending to amplify the moment response, regardless of the MLS principal direction. Out of the two, wave height appears to be the dominant driver of MLS magnitudes within the set of considered conditions. A slight exception to this is seen at the 35 m rotor height, which shows a considerable jump in MLS magnitude with wave period. The dominant variable may therefore be subject to change based on rotor position. These results also indicate that the effect of wave period is diminished as the rotor is positioned lower in the water column. This observation could prove useful when deciding on a turbine's designed operating location. Finally, these results show that the opposing wave cases yielded greater MLS magnitudes in comparison to their following wave counterparts.

With respect to the MLS principal direction results (Fig. 12, bottom), the plots have been shaded to indicate whether the cases are pitch or yaw dominant. The blue shaded regions indicate an out-of-plane rotor moment that cycles predominantly in M_y (pitch), and yellow indicates cycling predominantly in M_z (yaw). Note here also the exclusion of the no-wave cases. This is due to the circular nature of their moment traces, which causes the MLS principal direction to become arbitrary and uninformative. More generally, the same holds for all instances where moment traces are very circular. Within the MLS principal direction results it can be seen that, across the full set of simulations, shorter period waves tend to correspond to pitch-dominant load cycling while longer period waves result in yaw-dominant load cycling. This is consistent with the results of Fig. 10. However, there are exceptions to this broader trend, specifically the 8.5s wave cases at 25 m and 35 m rotor heights. This is understood to be due to the fact that load results in these cases fall somewhere between pitch and yaw-dominant load cycling, resulting in polar traces which are closer to circular and so the principal direction is less informative here. Furthermore, MLS principal direction plots demonstrate a clear sensitivity to wave direction. In the cases of following waves, the MLS principal directions

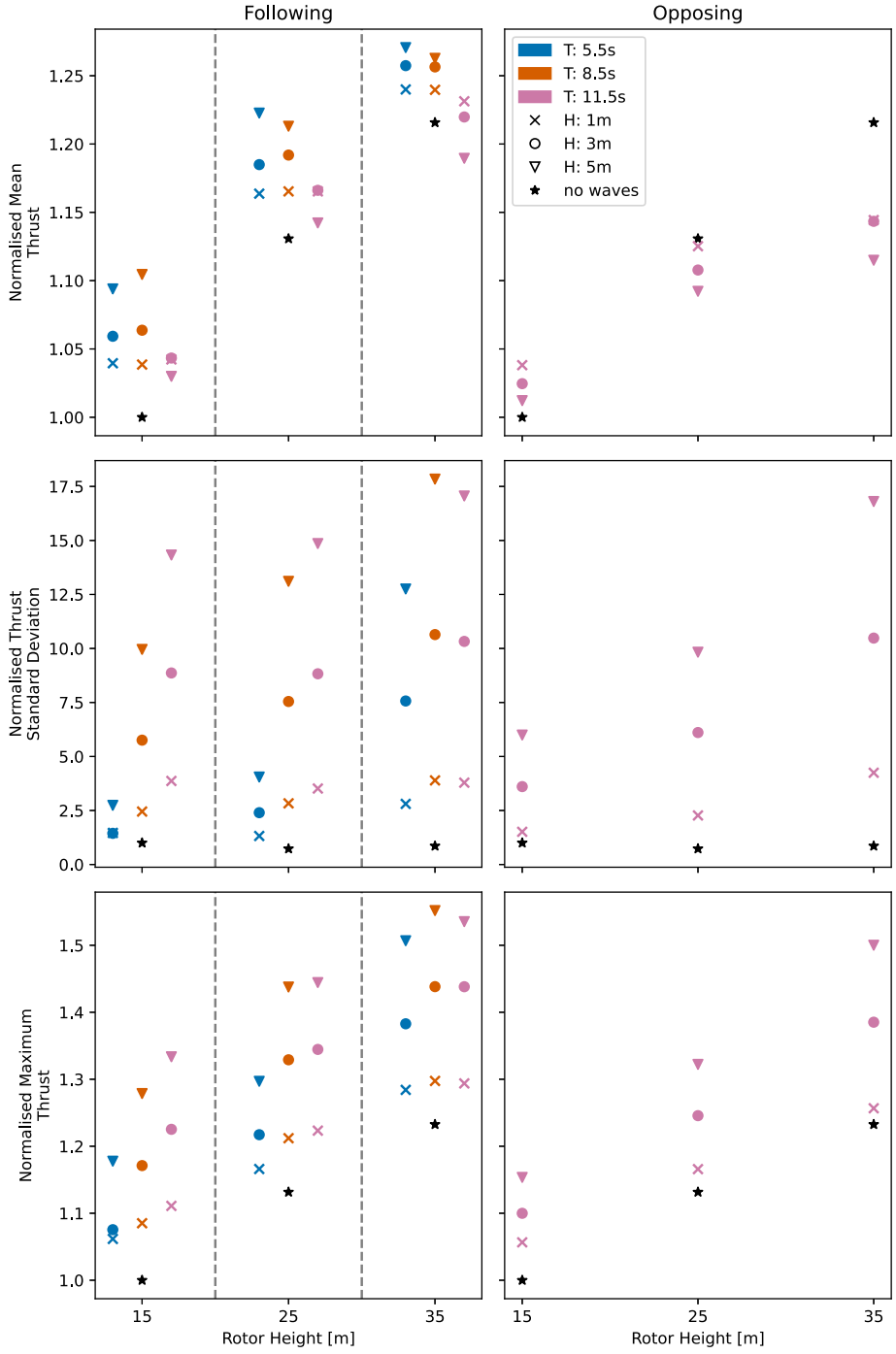

Fig. 13. Rotor thrust statistical scatter plots for all the simulated cases.

for the longest period wave falls exclusively within yaw-dominant load cycling regions, while in the opposing wave cases all but one fall within pitch-dominant regions. These results again highlight the sensitivities, complexities and myriad interactions that ultimately determine the resulting load conditions at the turbine hub, which then propagate into the drivetrain and turbine support structure. While this work has presented important advances with respect to our understanding of tidal turbine mechanical loading and flow interactions, it also serves to highlight that much additional work is required in order to facilitate optimal turbine design, location, and operation/control.

5. Conclusions

A numerical model of a turbine operating in a combined wave–current environment was developed and validated against tank testing data, showing good agreement for performance coefficients C_P and C_T across a range of TSRs. The rotor load response was further validated in the presence of waves, again showing good agreement. The model was subsequently linearly up-scaled to represent a full-scale 1.5 MW tidal turbine operating in a realistic ocean environment. A series of simulations were then performed in order to study the impacts of hub height and wave conditions on turbine mechanical rotor loads. The

key findings from the study showed that in cases of *following* waves, the mean torque and thrust are increased consistently as the rotor approaches free surface. Torque and thrust were also shown to increase with wave height up until the longest period wave, where a decrease then occurs. This was found to result from wave orbital velocities distorting the onset bulk flow-angle, producing a misalignment with the turbine rotor. Rotor loads were therefore found to be also dependent on wave period. The observed reduction in mean torque, for longer period waves, did not correspond to similar reductions in torque standard deviations or maximum values. In this case, the turbine is operating with an undesirable combination of reduced power and fatigue loads which remain essentially unchanged. *Opposing* wave cases showed a potential for decreases in torque and thrust responses as the hub height is moved higher in the column, and more significant changes in rotor loads were seen closer to the free surface. The presence of waves was shown to increase mean torque and thrust levels by up to 22% and 11% respectively. This corresponded to increases of 2500% and 1700% in signal standard deviations, and increases of 80% and 30% to maximum values for torque and thrust, respectively. A new metric, the Maximum Load Span (MLS), was developed to analyse the form and magnitude of cyclic out-of-plane rotor moment patterns. The MLS provides a useful metric for quantifying the variability in loading experienced by the rotor. The MLS was studied across the simulation package and was found to be increase with both hub height and wave height. There was also a seeming dependence on wave period, which changed the cyclic form of the out-of-plane moment patterns, leading to what has been referred to as "**wave-driven moment-type dominance**". Longer wave periods resulted in moment loading that was dominated by a yaw response, while shorter period waves resulted in a predominantly pitching moment response. Overall, the rotor position in the water column and wave composition were shown here to have a significant impact on tidal turbine rotor mechanical load response.

Declaration of competing interest

The authors declare that they have no known competing financial interests or personal relationships that could have appeared to influence the work reported in this paper.

Data availability

Data will be made available on request.

Acknowledgments

This work was funded by the UKRI through EP/R513349/1.

Appendix. Additional figures

See Fig. 13.

References

Allmark, M., Ellis, R., Porter, K., O'doherty, T., Johnstone, C., 2018. The development and testing of a lab-scale tidal stream turbine for the study of dynamic device loading. In: 4th Asian Wave and Tidal Energy Conference.

Apsley, D., Stallard, T., Stansby, P., 2018. Actuator-line CFD modelling of tidal-stream turbines in arrays. J. Ocean Eng. Mar. Energy 4, 259–271. http://dx.doi.org/10.1007/s40722-018-0120-3.

Arabian-Hoseynabadi, H., Oraee, H., Tavner, P.J., 2010. Failure modes and effects analysis (FMEA) for wind turbines. Int. J. Electr. Power Energy Syst. 32, 817–824. http://dx.doi.org/10.1016/j.ijepes.2010.01.019.

Bachant, P., Goude, A., Wosnik, M., 2016. Turbinesfoam: v0.0.7. http://dx.doi.org/10.5281/ZENODO.49422.

Bachant, P., Goude, A., Wosnik, M., 2018. Actuator line modeling of vertical-axis turbines. arXiv:1605.01449.

Bachant, P., Wosnik, M., 2015. Simulating wind and marine hydrokinetic turbines with actuator lines in RANS and LES. In: APS Division of Fluid Dynamics Meeting Abstracts. p. E28.003.

Blackmore, T., Myers, L.E., Bahaj, A.S., 2016. Effects of turbulence on tidal turbines: Implications to performance, blade loads, and condition monitoring. Int. J. Mar. Energy 14, 1–26. http://dx.doi.org/10.1016/j.ijome.2016.04.017.

Carroll, J., Koukoura, S., McDonald, A., Charalambous, A., Weiss, S., McArthur, S., 2019. Wind turbine gearbox failure and remaining useful life prediction using machine learning techniques. Wind Energy 22, 360–375. http://dx.doi.org/10.1002/we.2290.

Clarke, J.A., Connor, G., Grant, A.D., Johnstone, C.M., 2006. Regulating the output characteristics of tidal current power stations to facilitate better base load matching over the Lunar cycle. Renew. Energy 31, 173–180. http://dx.doi.org/10.1016/j.renene.2005.08.024.

Coles, D., Greenwood, C., Vogler, A., Walsh, T., Taaffe, D., 2018. Assessment of the turbulent flow upstream of the Meygen Phase 1A tidal stream turbines. Awtec.

de Jesus Henriques, T.A., Tedds, S.C., Botsari, A., Najafian, G., Hedges, T., Sutcliffe, C.J., Owen, I., Poole, R.J., 2014. The effects of wave– current interaction on the performance of a model horizontal axis tidal turbine. Int. J. Mar. Energy 8, 17–35. http://dx.doi.org/10.1016/j.ijome.2014.10.002.

Devolder, B., Rauwoens, P., Troch, P., 2017. Application of a buoyancy-modified k-$omega$ SST turbulence model to simulate wave run-up around a monopile subjected to regular waves using OpenFOAM®. Coast. Eng. 125, 81–94. http://dx.doi.org/10.1016/j.coastaleng.2017.04.004.

Devolder, B., Troch, P., Rauwoens, P., 2018. Performance of a buoyancy-modified k-$ømega$ and k-$ømega$ SST turbulence model for simulating wave breaking under regular waves using OpenFOAM®. Coast. Eng. 138, 49–65. http://dx.doi.org/10.1016/j.coastaleng.2018.04.011.

Draper, S., Adcock, T.A.A., Borthwick, A.G.L., Houlsby, G.T., 2014. Estimate of the tidal stream power resource of the pentland firth. Renew. Energy 63, 650–657. http://dx.doi.org/10.1016/j.renene.2013.10.015.

Draycott, S., Payne, G., Steynor, J., Nambiar, A., Sellar, B., Venugopal, V., 2019. An experimental investigation into non-linear wave loading on horizontal axis tidal turbines. J. Fluids Struct. 84, 199–217. http://dx.doi.org/10.1016/j.jfluidstructs.2018.11.004.

Drela, M., 1989. XFOIL: An Analysis and design system for low Reynolds number airfoils. In: Brebbia, C.A., Orszag, S.A., Seinfeld, J.H., Spanos, P., Cakmak, A.S., Silvester, P., Desai, C.S., Pinder, G., McCrory, R., Yip, S., Leckie, F.A., Ponter, A.R.S., Holz, K.P., Bathe, K.J., Connor, J., Wunderlich, W., Argyris, J., Mueller, T.J. (Eds.), Low Reynolds Number Aerodynamics, vol. 54. Springer Berlin Heidelberg, Berlin, Heidelberg, pp. 1–12. http://dx.doi.org/10.1007/978-3-642-84010-4_1.

Edinburgh Compute and Data Facility website, 2023. University of Edinburgh. www.ecdf.ed.ac.uk.

Faudot, C., Dahlhaug, O.G., 2012. Prediction of wave loads on tidal turbine blades. Energy Procedia 20, 116–133. http://dx.doi.org/10.1016/j.egypro.2012.03.014.

Galloway, P., Myers, L., Bahaj, A.S., 2014. Quantifying wave and yaw effects on a scale tidal stream turbine. Renew. Energy 63, 297–307. http://dx.doi.org/10.1016/j.renene.2013.09.030.

Gaurier, B., Carlier, C., Germain, G., Pinon, G., Rivoalen, E., 2020. Three tidal turbines in interaction: An experimental study of turbulence intensity effects on wakes and turbine performance. Renew. Energy 148, 1150–1164. http://dx.doi.org/10.1016/j.renene.2019.10.006.

Gaurier, B., Davies, P., Deuff, A., Germain, G., 2013. Flume tank characterization of marine current turbine blade behaviour under current and wave loading. Renew. Energy 59, 1–12. http://dx.doi.org/10.1016/j.renene.2013.02.026.

Gaurier, B., Germain, G., Facq, J.V., Johnstone, C.M., Grant, A.D., Day, A.H., Nixon, E., Di Felice, F.., Costanzo, M., 2015. Tidal energy round Robin tests comparisons between towing tank and circulating tank results. Int. J. Mar. Energy 12, 87–109. http://dx.doi.org/10.1016/j.ijome.2015.05.005.

Guo, Y., Bankestrom, O., Bergua, R., Keller, J., Dunn, M., 2021. Investigation of main bearing operating conditions in a three-point mount wind turbine drivetrain. Forschung im Ingenieurwesen 85.

Guo, Y., Keller, J., 2018. Investigation of high-speed shaft bearing loads in wind turbine gearboxes through dynamometer testing. Wind Energy 21, 139–150.

Guo, X., Yang, J., Gao, Z., Moan, T., Lu, H., 2018. The surface wave effects on the performance and the loading of a tidal turbine. Ocean Eng. 156, 120–134. http://dx.doi.org/10.1016/j.oceaneng.2018.02.033.

Hart, E., 2020. Developing a systematic approach to the analysis of time-varying main bearing loads for wind turbines. Wind Energy 23, 2150–2165.

Hart, E., Clarke, B., Nicholas, G., Kazemi Amiri, A., Stirling, J., Carroll, J., Dwyer-Joyce, A., Long, H., 2020. A review of wind turbine main bearings: Design, operation, modelling, damage mechanisms and fault detection. Wind Energy Sci. 5, 105–124. http://dx.doi.org/10.5194/wes-5-105-2020.

Hart, E., Stock, A., Elderfield, G., Elliott, R., Brasseur, J., Keller, J., Guo, Y., Song, W., 2022. Impacts of wind field characteristics and non-steady deterministic wind events on time varying main-bearing loads. Wind Energy Sci. 1–28.

Hart, E., Turnbull, A., Feuchtwang, J., McMillan, D., Golysheva, E., Elliott, R., 2019. Wind turbine main-bearing loading and wind field characteristics. Wind Energy 22, 1534–1547. http://dx.doi.org/10.1002/we.2386.

Higuera, P., 2018. Phicau/olaFlow: CFD for waves. Zenodo, http://dx.doi.org/10.5281/zenodo.1297013.

Larsen, B.E., Fuhrman, D.R., 2018. On the over-production of turbulence beneath surface waves in Reynolds-averaged Navier–Stokes models. J. Fluid Mech. 853, 419–460. http://dx.doi.org/10.1017/jfm.2018.577.

Lewis, M., Neill, S.P., Robins, P., Hashemi, M.R., Ward, S., 2017. Characteristics of the velocity profile at tidal-stream energy sites. Renew. Energy 114, 258–272. http://dx.doi.org/10.1016/j.renene.2017.03.096.

Liu, L., Franceschini, L., Oliveira, D.F., Galeazzo, F.C., Carmo, B.S., Stevens, R.J., 2022. Evaluating the accuracy of the actuator line model against blade element momentum theory in uniform inflow. Wind Energy 1046–1059. http://dx.doi.org/10.1002/we.2714.

Liu, Z., Zhang, L., 2020. A review of failure modes, condition monitoring and fault diagnosis methods for large-scale wind turbine bearings. Meas.: J. Int. Meas. Confeder. 149, 107002. http://dx.doi.org/10.1016/j.measurement.2019.107002.

Lust, E., Luznik, L., Flack, K.A., Walker, J., Van Benthem, M., 2013. The influence of surface gravity waves on marine current turbine performance. Int. J. Mar. Energy 2013, 27–40. http://dx.doi.org/10.1016/j.ijome.2013.11.003.

Luznik, L., Flack, K.A., Lust, E., Taylor, K., 2013. The effect of surface waves on the performance characteristics of a model tidal turbine. Renew. Energy 58, 108–114. http://dx.doi.org/10.1016/j.renene.2013.02.022.

Martinez, R., Payne, G.S., Bruce, T., 2018. The effects of oblique waves and currents on the loadings and performance of tidal turbines. Ocean Eng. 164, 55–64. http://dx.doi.org/10.1016/j.oceaneng.2018.05.057.

Medina, O.D., Schmitt, F.G., Calif, R., Germain, G., Gaurier, B., 2017. Turbulence analysis and multiscale correlations between synchronized flow velocity and marine turbine power production. Renew. Energy 112, 314–327. http://dx.doi.org/10.1016/j.renene.2017.05.024.

Mendoza, V., Bachant, P., Wosnik, M., Goude, A., 2016. Validation of an actuator line model coupled to a dynamic stall model for pitching motions characteristic to vertical axis turbines. J. Phys. Conf. Ser. 753, 1–12. http://dx.doi.org/10.1088/1742-6596/753/2/022043.

Mendoza, V., Goude, A., 2017. Wake flow simulation of a vertical axis wind turbine under the influence of wind shear. J. Phys. Conf. Ser. 854, 1–11. http://dx.doi.org/10.1088/1742-6596/854/1/012031.

Mendoza, V., Goude, A., 2020. Validation of actuator line and vortex models using normal forces measurements of a straight-bladed vertical axis wind turbine. Energies (13), http://dx.doi.org/10.3390/en13030511.

Mycek, P., Gaurier, B., Germain, G., Pinon, G., Rivoalen, E., 2014. Experimental study of the turbulence intensity effects on marine current turbines behaviour, part I: One single turbine. Renew. Energy 66, 729–746. http://dx.doi.org/10.1016/j.renene.2013.12.036.

Nejad, A.R., Keller, J., Guo, Y., Sheng, S., Polinder, H., Watson, S., Dong, J., Qin, Z., Ebrahimi, A., Schelenz, R., et al., 2022. Wind turbine drivetrains: State-of-the-art technologies and future development trends. Wind Energy Sci. 7, 387–411.

Noble, D., Davey, T., Smith, H., Kaklis, P., Robinson, A., Bruce, T., 2015. Spatial variation of currents generated in the FloWave ocean energy research facility. In: European Wave and Tidal Energy Conference. p. 9.

Noble, D.R., Draycott, S., Nambiar, A., Sellar, B.G., Steynor, J., Kiprakis, A., 2020. Experimental assessment of flow, performance, and loads for tidal turbines in a closely-spaced array. Energies (13), http://dx.doi.org/10.3390/en13081977.

Onel, H.C., Tuncer, I.H., 2020. A comparative study of wake interactions between wind-aligned and yawed wind turbines using les and actuator line models. J. Phys.: Conf. Ser. 1618. http://dx.doi.org/10.1088/1742-6596/1618/6/062009.

Ordonez-Sanchez, S., Allmark, M., Porter, K., Ellis, R., Lloyd, C., Santic, I., O'Doherty, T., Johnstone, C., 2019. Analysis of a horizontal-axis tidal turbine performance in the presence of regular and irregular waves using two control strategies. Energies (12), http://dx.doi.org/10.3390/en12030367.

Payne, G.S., Stallard, T., Martinez, R., 2017. Design and manufacture of a bed supported tidal turbine model for blade and shaft load measurement in turbulent flow and waves. Renew. Energy 107, 312–326. http://dx.doi.org/10.1016/j.renene.2017.01.068.

Perez, L., Cossu, R., Grinham, Alistair, Penesis, Irene, 2022. Tidal turbine performance and loads for various hub heights and wave conditions using high-frequency field measurements and blade element momentum theory. Renew. Energy 200, 1548–1560. http://dx.doi.org/10.1016/j.renene.2022.10.058.

Stirling, J., Hart, E., Kazemi Amiri, A., 2021. Constructing fast and representative analytical models of wind turbine main bearings. Wind Energy Sci. 6, 15–31.

Tatum, S.C., Frost, C.H., Allmark, M., O'Doherty, D.M., Mason-Jones, P.W., Grosvenor, R.I., Byrne, C.B., O'Doherty, T., 2016. Wave–current interaction effects on tidal stream turbine performance and loading characteristics. Int. J. Mar. Energy 14, 161–179. http://dx.doi.org/10.1016/j.ijome.2015.09.002.

Troldborg, N., Sørensen, J.N., Mikkelsen, R., 2007. Actuator line simulation of wake of wind turbine operating in turbulent inflow. J. Phys.: Conf. Ser. 75. http://dx.doi.org/10.1088/1742-6596/75/1/012063.

Weller, H.G., Tabor, G., Jasak, H., Fureby, C., 1998. A tensorial approach to computational continuum mechanics using object-oriented techniques. Comput. Phys. 12 (620), http://dx.doi.org/10.1063/1.168744.